Behavior of the square-back Ahmed body global modes at low ground clearance

Baptiste Plumejeau,[1,2,3] Laurent Keirsbulck,[1,2,*] Sébastien Delprat,[1,2]
Marc Lippert,[1,2] and Wafik Abassi[3]
[1]*Université Polytechnique Hauts-de-France, Umr 8201-Lamih, F-59313 Valenciennes, France*
[2]*Cnrs Umr 8201, F-59313 Valenciennes, France*
[3]*Ipsa, 63 Boulevard de Brandebourg, F-94200 Ivry-sur-Seine, France*

(Received 9 April 2020; accepted 10 July 2020; published 26 August 2020)

The present work aims to study the evolution of the wake-flow dynamic, including the shear-layers interactions phenomena and the global modes behavior of a square-back Ahmed body with a width to height aspect ratio, w/h, of 1.346. Various ground-clearance configurations around the critical case associated with the onset of the lateral bistability and corresponding to a critical ground clearance, $g_c/w = 0.1$, are investigated. For this purpose, vertical and transversal planar particle image velocimetry (PIV) and concurrent base pressure and force measurements are performed. Results show that the instantaneous wake-flow interactions between the side- or under-body flow and the wake shear layers depend mainly on the under-body flow rate and that a particular attention is required for the experimental under-body flow conditions. Pressure-velocity correlations and instantaneous filtered PIV snapshots analysis highlight the preferential shear-layer vortex shedding associated with the two selected stable and bistable wake-flow configurations. Present investigations underline the transition process from a stable wake configuration ($g/w < 0.1$) to a bistable state flow configuration ($g/w > 0.1$). The antisymmetric periodic global mode is strongly affected around the critical bistable case at the origin of a substantial drag reduction. The oscillation modes varies between stable and bistable states, and then the corresponding Strouhal numbers for the horizontal (respectively, vertical) evolve from 0.16 (respectively, 0.27) to 0.13 (respectively, 0.18). With regard to the present space-time evolution of the wake-flow features, a dynamical interpretation of the different interactions mechanisms is finally proposed for each case with a particular interest to the low-ground-clearance configurations poorly described in the literature.

DOI: 10.1103/PhysRevFluids.5.084701

I. INTRODUCTION

Improving personal vehicle energetic performances has become a priority nowadays. Several approaches can be considered, such as power-train hybridization or electrification. During highway driving conditions, aerodynamic losses are the most important source of energy consumption [1]. In these conditions, the development of flow control strategies based on the flow physics (physics-based control) requires a thorough understanding of the wake flow of the considered bluff body with regards to its contribution to the aerodynamic drag. It is thus necessary to characterize accurately the complex unsteady and three-dimensional aerodynamical fields and to educe the flow mechanisms responsible for the generation of significant pressure fluctuations in the wake. Since a couple of years, numerous studies have examined the flows around the so-called Ahmed body [2]

*laurent.keirsbulck@uphf.fr

providing a generic representation of a road vehicle, including the essential features of the flow field such as three-dimensional separation and ground-clearance effect. Indeed, more generally, when a bluff-body is placed in the proximity of a solid wall, the dynamical behavior of the wake-flow changes significantly as a function of the obstacle-to-wall gap height, when compared to the same geometry in a uniform stream. The wake of this kind of bluff body presents weak coherent oscillations in the vertical and lateral directions, so called global modes [3], as it the case for cylinders in cross-flow. They are generally considered to be the result of separated shear-layers Kelvin–Helmholtz instabilities coupling. The presence of global modes in wakes of such flows could impact significantly the drag. As a consequence, an efficient control able to disturb the global modes as for example spanwize cylinders placed on the top, the bottom or in the wake of the body (Ahmed body [4] and D-shape [5]) can lead to an increase of the recirculation length and substantial drag reductions. This partially explains the recent enthusiasm of research in the field [6–8]. The natural wake dynamics of a square-back Ahmed body is subject to drastic changes when the ground clearance reaches a critical value, g_c. This variation of the flow dynamic behavior is due to the onset of strong horizontal static mode with large timescale. In this case, the wake flips between two asymmetric steady states (named wake symmetry breaking (WSB) states). In the long-time average this "flipping" leads to a statistically symmetric wake, while instantaneously it is typically asymmetric. This bistability phenomenon was first recognized by Herry *et al.* [9], who observed mean flow asymmetry for flows over a three-dimensional double backward-facing step. Since then, number of studies have examined this feature in various bluff body configurations [3,10], including the square-back Ahmed body [11–16]. In this framework, Cadot *et al.* [17], studied the effects of both the wall proximity and the Reynolds number, and demonstrated that the bimodal behavior is the result of an imperfect pitchfork bifurcation with two branches corresponding to the WSB states. This static global mode appears after the first steady instability in the laminar regime as described experimentally by Grandemange *et al.* [12] and numerically by Evstafyeva *et al.* [7]. These authors reveal that the low-Reynolds-number bifurcation sequence leads to a symmetry breaking of the wake. It persists at turbulent high Reynolds numbers with a bimodal behavior and random switching between the asymmetric states. This flipping behavior is the way for the system to restore the experimental reflectional symmetry. These authors conjectured that this change in the flow happens once there is sufficient under-body flow, allowing the shear-layers shed from the top and bottom of the base to interact together. These changes are accompanied by a drag reduction. The complexity of wake dynamics and its control stay a real challenge since the wake organization is then the combination of energetic oscillating global modes and convective co-rotating vortices shedding induced by Kelvin–Helmholtz instabilities associated with each shear-layer. Moreover, these last coherent dynamics are generally difficult to observe mainly due to their low energetic footprint and could not be clearly evidenced in the spatial domain. Overall, most of the previous studies focused on the large ground clearance where the wake flow is bistable. In this case, the antisymmetric horizontal (respectively, vertical) periodic global modes have Strouhal numbers for oscillation of 0.13 (respectively, 0.18.) [13]. The aim of the present work is to describe the significant wake dynamic changes near the critical point where the bistability (also called bimodality) appears. Close to this critical point, the under-body flow rate level induces strong horizontal shear-layer interactions variations and modifies the global modes behavior. As a consequence the drag is significantly reduced. A comparison of the main dynamic features, including the shear-layer interactions, before and after the onset of wake symmetry breaking state, with a particular interest on the global modes behavior is addressed.

For this purpose, the outline of the paper is as follow: Sec. II describes the setup and the measurement techniques. Section III is related to the global flow description and aims to select the experimental cases used in the following part of the present paper. A literature review is first presented and underlines the dependency on the drag to various parameters, such as the ground clearance, the w/h aspect ratio, and the Reynolds numbers effect. A focus on the importance of the model support is also addressed. Section IV is devoted to the dynamical analysis of the wake-flow interactions with regards to the ground clearance for a given Reynolds number of

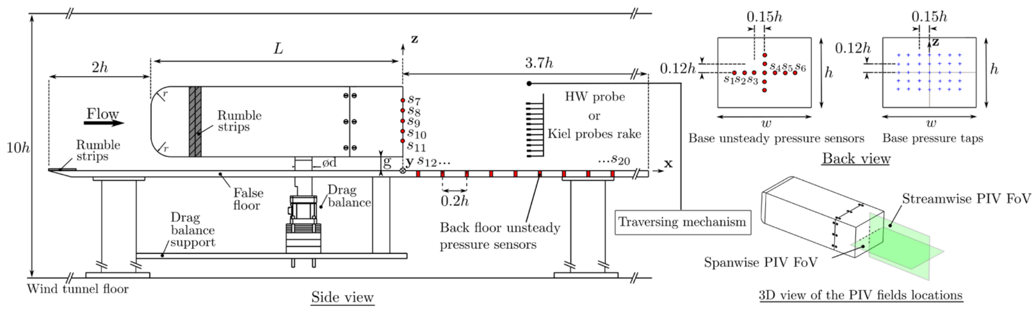

FIG. 1. Sketch of the experimental setup with PIV fields and base pressure sensors locations.

2.86×10^5. The drastic flow changes near the critical point are analyzed using combined wall pressure/velocity measurements and provides a detailed description of the dynamical coupling between under-body/lateral flow and the shear-layers. In Sec. V, a global discussion about the oscillating modes with regards to the stable and bistable wake-flow states is proposed. Finally, conclusive remarks end the paper with an interpretation for the dynamical wake behavior.

II. EXPERIMENTAL DETAILS

The present experiment was performed in the LAMIH closed-circuit subsonic wind-tunnel with a 6.25:1 contraction ratio. The 10-m-long working section has a $2 \times 2\,\mathrm{m}^2$ cross-sectional area and the free-stream turbulent intensity is less that 0.6% in the present range of studied velocities. The Ahmed body model shown in Fig. 1 was centered between the side walls, the ceiling, and the floor within the test section. The geometry is placed in wall proximity with a plate up-raised from the wall of the tunnel. The coordinate system is defined as **x** in the streamwise direction, **z** normal to the ground, and **y** in the lateral direction as shown in Fig. 1. The bluff body geometry has a width, w of 272 mm and a height, h of 202 mm, leading to an aspect ratio, w/h of 1.346 and a length, L of 730 mm, the cylindrical central support has a diameter of 50 mm. The radius of the rounding of the fore-body, r is 29 mm. The support mast is especially designed to avoid body vibrations and to have a natural shedding frequency out of the range of the wake global modes. The body is made of two blocs, the leading first part is linked to the drag balance attachment, while the second back part contains the surface-pressure probes. The ground clearance of the geometry, denoted by g can be precisely set up to 50 mm with a micrometric traverse device. It corresponds to the original Ahmed body [2] configuration with a scale of 0.7. To thicken the turbulent boundary layer, a 35-mm-wide strip is installed at the beginning of the flat plate and on the front part of the Ahmed body. Based on the height of the model, the Reynolds number of this flow is defined as $\mathrm{Re}_h = U_\infty.h/\nu$, where ν is the kinematic viscosity of the air at ambient temperature and U_∞ the free-stream velocity. Experiments are conducted for three different free-stream velocities, U_∞ of 10, 20 and 30 m/s, corresponding to $\mathrm{Re}_h = 1.43 \times 10^5$, 2.86×10^5 and 4.29×10^5, respectively.

For unsteady pressure analysis, the model base and the floor in the wake are instrumented with subminiature piezo-resistive Kulite XCQ-080 sensors allowing an effective measurement range of 35 kPa and a static accuracy of $\pm 0.1\%$ full scale output (fso). Eleven flush-mounted Kulite sensors are located at the back of the Ahmed body in the **z** and **y** midplane and nine on the back floor in the streamwise direction as shown in Fig. 1. For each experiment, unsteady pressure signals are sampled at 2 kHz with a cutoff frequency of 1 kHz for a total duration of 800 s. Thirty-five taps are distributed at the back of the body to get the repartition of base pressure field (Fig. 1). The pressure is obtained using a 64-port miniature Scanivalve MPS4264 pressure scanner (effective measurement range of 2000 Pa) with a static accuracy of $\pm 0.1\%$ fso corresponding to $\pm 3\,\mathrm{Pa}$. The pressure scanner takes 20 pressure samples per second and per channel and the measurement is automatically averaged over 1 s. The pressure scanner is located inside the model so that it is linked to each tap with less than 150 mm of vinyl tube to limit the filtering effect of the tubing. In the following, the pressure coefficient is calculated by $C_p = (p - p_\infty)/p_{\text{dyn}}$, with $p_{\text{dyn}} = \frac{1}{2}\rho U_\infty^2$ and where p_∞ denotes the reference static pressure and ρ the air density, measured from the pressure averaged over the blunt base surface. The base suction coefficient can be obtained by integration of the pressure coefficient at the base of the body as $C_b = -\frac{1}{A}\int_A C_p dA$, where A is the base surface including the probes. In our case, since the static pressures are only measured in the center region of the base and not on the entire base surface, the corresponding base suction coefficient can be considered only as a good estimation on the real C_b. Besides, the static pressure in the wake is measured through a rake composed of the eleven Kiel probes mounted on three-dimensional displacement systems (with a precision better than 0.1 mm). Kiel Probes are connected to a Furness controls scanner system composed of a FCS412 pressure scanner and a FCO560 manometer with an effective measurement range of 2000 Pa and a static accuracy of $\pm 0.1\%$ fso corresponding to ± 3 Pa. A three-dimensional mapping of the static pressure is obtained moving the Kiel rake by steps of $0.1h$ in both streamwise and spanwise directions. To quantify the global aerodynamic drag and side forces, a six-component Delta ATI balance (MC-3A model 500) with a sensing range of 0 to 1100 N. A static accuracy of $\pm 0.2\%$ fso is achieved. The global drag coefficient (respectively, the side-force coefficient, C_y), obtained from our drag balance, is defined by $C_D = F_x/(S.p_{\text{dyn}})$, where F_x is the measured drag force (respectively, F_y the side force) and S the projected frontal body area. A single hot-wire probe is used to measure the local velocities to extract the global mode frequencies. This hot-wire probe is mounted on a three-dimensional displacement system made up of 3D-traverse system with a precision better than 0.1 mm, operated by the Dantec Steamline 90N10 software.

The particle image velocimetry (PIV) measurements are carried out with a standard two-component TSI system, composed of a double-pulse 200 mJ dual-head ND-YAG (Quantel BSLT220) laser system and high-resolution CCD Powerview camera with a full resolution of 2048×2048 pixels and micro NIKKOR 50-mm optical lens. The seeding is generated using a TSI oil droplet atomizer 9307 with a mean droplets diameter, d_p of 1 μm. The seeding is released in the settling chamber of the wind tunnel. The relaxation time, τ_p of the seeding particles, defined as $\rho_p d_p^2/(18\mu_f)$, where μ_f is the air dynamic viscosity and ρ_p is the oil density (900 kg/m^3), is estimated to be 0.3μs. The Stokes number, $\text{St}_k = \tau_p/\tau_f$ (where τ_f is the characteristic timescale of the smallest eddies), must be less than 1 for the particles to faithfully follow the flow. The characteristic time considered here is the Kolmogorov timescale $\tau_f = \sqrt{\nu/\epsilon}$ (where ϵ is the kinetic energy dissipation) which is approximately 0.6 ms. This results in a Stokes number of 0.5×10^{-2}, indicate that droplet particles track the velocity fluctuations in the flow fairly well. The vector fields are obtained by processing the PIV images using a recursive cross-correlation algorithm with a final interrogation window size of 16×16 pixels with 50% overlap. The resulting PIV fields of view passing through the middle planes of the Ahmed body as mentioned in Fig. 1 are for the lateral plane about $2h \times 2.75h$ and about $1.6h \times 2.5h$ for the other one. For every test case (reported in Table III), 5000 time-uncorrelated PIV snapshots are recorded with a repetition rate of 7 Hz. The relative uncertainties on the mean velocities is estimated to 0.2% of the free stream velocity by using the methodology proposed by Charonko and Vlachos [18]. For time-space analysis purpose, the pressure and force readings are synchronized with the PIV measurements using a TTL signal triggered by a Q-switch of the first laser cavity. The Q-switch is acquired at 20 kHz simultaneously with the pressure measurements with a 12 bit A/D converter from a Dewesoft Sirius-8STG M plus acquisition system. Force measurements are low-pass filtered using a zero-phase digital filter to reduce noise and to preserve the temporality of the signals. The wake-flow degrees of asymmetry in the **x-y** plane are quantified by the horizontal pressure gradient $\partial C_p/\partial y^*$, between the s_1 and s_6 pressure sensors (Fig. 1). In the following, the superscript $*$ denotes the normalization by the free-stream velocity, U_∞ and/or the Ahmed body height, h.

TABLE I. Literature data sets compiled for analysis. B_u denotes the under-body support obstructivity.

Authors	h	w	w/h	$10^{-4}\mathrm{Re}_h$	Support type	B_u (%)	g/w	C_D	C_b
Ahmed *et al.* [2]	0.288	0.389	1.350	12.6	4 cyl.-feets	11	0.129	0.250	0.183
Volpe *et al.* [19][a]	0.288	0.389	1.350	51.0	4 plate-feets	10	0.129	0.324	0.239
	0.288	0.389	1.350	77.0		10	0.129	0.317	0.242
Grandemange *et al.* [3,20][a]	0.072	0.097	1.350	9.2	4 cyl.-feets	13	0.129	0.274	0.185
Eulalie *et al.* [21]	0.202	0.272	1.346	40.4	4 feets and a mast	29	0.249	0.364	0.215
Evrard *et al.* [22]	1.152	1.555	1.350	250.0	4 wheels	23	0.122	0.317	0.212
Li *et al.* [23]	0.297	0.350	1.178	20.0	4 profiled-feets	11	0.143	0.343	0.236
	0.297	0.350	1.178	30.0		11	0.143	0.306	0.235
	0.297	0.350	1.178	40.0		11	0.143	0.286	0.232
Barros *et al.* [24]	0.297	0.350	1.178	20.0	4 profiled-feets	11	0.143	0.308	0.204
	0.297	0.350	1.178	30.0		11	0.143	0.293	0.201
	0.297	0.350	1.178	40.0		11	0.143	0.269	0.196
Lucas *et al.* [25][b]	0.297	0.350	1.178	40.0	4 NACA0025-feets	11	0.085	0.356	0.188
Bonnavion and Cadot [26]	0.298	0.350	1.174	40.0	4 cyl.-feets	8	0.168	0.287	0.183

[a]Additional data are also available in the paper.
[b]Numerical study.

III. GLOBAL WAKE-FLOW DESCRIPTION

In this section, the global wake-flow properties are described with regards to the literature. First, the main key parameters influencing the onset of the bistability phenomenon are discussed with a particular interest on the under-body flow rate according to the ground clearance. Then, based on the previous analysis, the critical ground clearance is determined and the five selected PIV test cases reported in Table III are introduced to investigate the various wake-flow interactions acting on the global drag.

A. Global flow parameters

Before analyzing the wake-flow dynamics, a brief description of the present wake-flow characteristics is detailed hereafter. The boundary layers thickness just at the rear edges of the body is extracted from the various PIV measurements and reported in Table II for the three Reynolds numbers studied. The values are slightly lower that those found by Barros *et al.* [27], but they can be easily explained by the different aspect ratios, w/h and the total length, L of the Ahmed body. The pressure field in the wake of the body is also analyzed for $\mathrm{Re}_h = 2.86 \times 10^5$ and $g/w = 0.154$ to have an idea of the pressure losses area. Fig. 2 shows the zero pressure coefficient isosurface and the contours of pressure in the middle plane **x-z**. The minimal pressure in the wake are located inside the recirculation region and correspond to the mean vortex cores (see Fig. 2). The adverse pressure gradient is particularly intense on the ground and induces significant losses of momentum on the ground downstream of the body as mentioned previously by Grandemange *et al.* [13].

TABLE II. Upper and lateral boundary layer thickness against Reynolds numbers with corresponding C_b and C_D symbols used in Fig. 3 for $g/w = 0.154$.

$10^{-5}\mathrm{Re}_h$	C_D	C_b	$\delta^*_{99\text{-lateral}}$	$\delta^*_{99\text{-upper}}$
1.43	● (blue)	+ (blue)	0.133	0.145
2.86	● (red)	+ (red)	0.097	0.106
4.29	● (red)	+ (red)	0.075	0.090

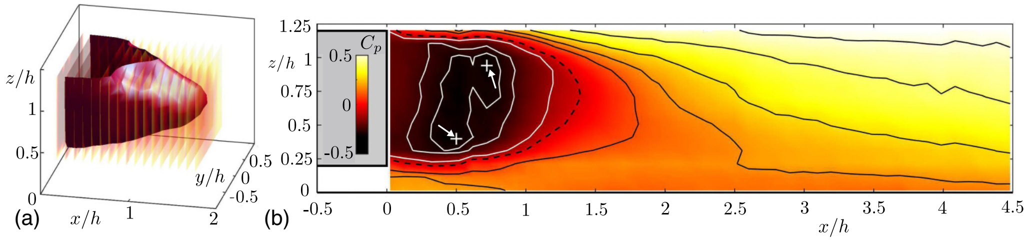

FIG. 2. Static pressure measurements in the wake for $\mathrm{Re}_h = 2.86 \times 10^5$ and with $g/w = 0.154$. (a) Zero-pressure coefficient isosurface, (b) contours of static pressure in the plane **y**-**z**. Continuous black and white lines refers to positive and negative values, zero contour is denoted by dotted-dashed line and contour intervals are 0.1. Local minimum of mean pressure coefficient are located by the two white arrows.

Moreover, the far-field pressure distribution (Fig. 2) is not disturbed by the present raised-floor end (located at $3.7h$).

The present global drag measurements are compared to those obtained from the literature reported in Table I and a discussion on the main factors inducing discrepancies is addressed. To this purpose, the Reynolds numbers dependence of the drag coefficients is first presented in Fig. 3 for large ground clearance ($g/w > 0.1$). The present data fit well with Volpe *et al.* [19] and globally with the data sets with the same w/h ratio ($\approx$1.350). A fitting curve through the present data including the values reported in Table I for $w/h \approx 1.350$ has been plotted and can be extended over one order of Reynolds number magnitude. For $\mathrm{Re}_h > 3 \times 10^5$, the drag coefficients are less Reynolds number dependent and tend towards the value of 0.317 given by Evrard *et al.* [22] for their industrial Ahmed body large scale study. We can notice that the C_D obtained in the lowest Reynolds number studies are lower, probably due to Reynolds number effect (see Fig. 3). Similar trends, with a shift, can be observed with the data set reported in Table I for the aspect ratios $w/h \approx 1.178$. Concerning the base suction coefficient, depicted in Fig. 3, a slight increasing against the Reynolds numbers can also be observed. A scattering of the drag and base suction measurements can be observed. The test section blockage for all the reported cases are relatively low and does not permit to explain the strong observed drag variations. The under-body support obstructivity can partially explain this

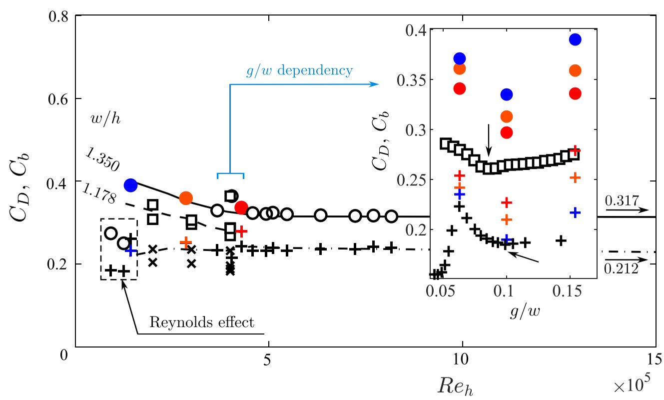

FIG. 3. Global drag (○ for $w/h \approx 1.350$ or □ for $w/h \approx 1.178$) and base suction (+ for $w/h \approx 1.350$ or × for $w/h \approx 1.178$) coefficients against Reynolds numbers from Table I with the present measurements for $g/w = 0.154$ (reported in Table II). Subfigure shows the present global drag and base suction coefficients against g/w. Data from Bonnavion *et al.* [28] and Grandemange *et al.* [3] are also added. The black arrows highlights the minimum drag.

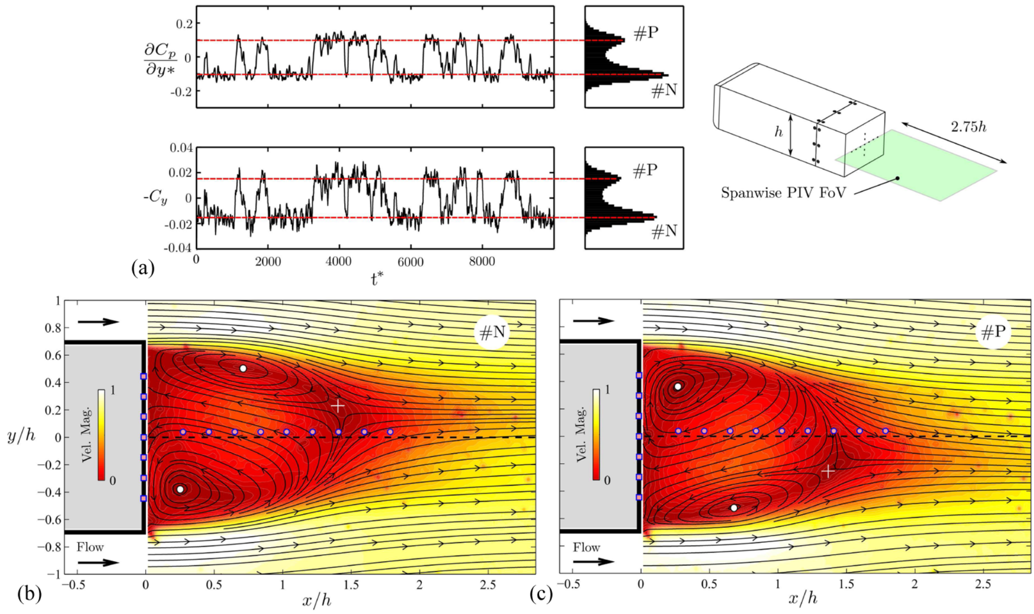

FIG. 4. (a) Time histories and PDFs of the horizontal pressure gradient and the side-force coefficient for $g/w = 0.154$ and $\mathrm{Re}_h = 2.86 \times 10^5$, (b) #$N$ and (c) #P associated conditional averaging velocity fields. The white cross denotes the saddle point while the white circle denotes the vortex cores. The pink symbols denote the pressure probes location.

scattering and especially the higher drag values (due to the presence of the central mast leading to an under-body support obstructivity of 15%). This is confirmed by relatively high obstructivity studies (i.e., Eulalie *et al.* [21] and Evrard *et al.* [22]). As mentioned in the study of Bonnavion *et al.* [28], the ground clearance affects the drag values (through the under-body flow rate variation) and can explain the other discrepancies observed in the literature when the Reynolds number and a w/h ratio are fixed. The subfigure included in Fig. 3 shows the evolution of the drag and base suction coefficients against the ground clearance for the present and from Bonnavion *et al.* [28] and Grandemange *et al.* [3] measurements for comparison. These authors observe a drag decrease when g/w is lower than a critical value ($g/w = 0.08$ for $w/h = 1.178$ and $g/w = 0.1$ for $w/h = 1.35$) and a slight increase for higher values. This tendency is supported by our data. Consequently, our data fits well with most of the previous works and underlines a substantial ground-clearance effect potentially interesting as a flow mechanism able to reduce the drag. This point will be under investigation in Sec. IV.

B. Onset of the symmetry breaking

As now clearly known, the ground-clearance effect on the global drag force can be linked to strong wake topology modifications. In particular, the turbulent wake of a square-back body exhibits a strong bimodal behavior. This bistable behavior is typically encountered in many three-dimensional bluff body [9] or axisymmetric flow configurations [14]. This phenomenon is clearly visible, in the transverse direction, for the present case of an Ahmed body with an aspect ratio of $w/h = 0.135$ as previously observed in the literature [3,13,20,27–29]. Classically, the time history of the horizontal pressure gradient or the C_y coefficient highlights a switching behavior between two distinct stable levels clearly visible on Fig. 4(a). The associated PSD reveals different characteristic frequencies corresponding to two very distinctive timescales as observed in the literature [13,19]; a long timescale $T_{\mathrm{WSB}} \propto 10^3.h/U_\infty$, linked to the switching behavior between two static modes and a short timescales $T_{\mathrm{Sh}} \propto 5.w/U_\infty$, corresponding to a lateral periodic global antisymmetric

TABLE III. Main parameters of the present PIV test cases

$10^{-5}\mathrm{Re}_h$	g/w	U_s^*	q_s^*	C_D	C_b
2.86[a]	0.063	0.37	0.031	0.361	0.242
2.86	0.100	0.46	0.066	0.313	0.210
2.86[b]	0.154	0.57	0.099	0.359	0.252
1.43	0.100	0.39	0.056	0.335	0.192
4.29	0.100	0.49	0.070	0.297	0.227

[a]Stable reference case.
[b]Bi-stable reference case.

mode as discussed later. The characteristic time for reversals is about 2 orders of magnitude larger than the other one. Before analyzing in detail the onset of the wake-flow bistability, we define the two flow states by applying a conditional averaging ($\mathbf{u}_{\#P} = \langle \mathbf{u} | \partial C_p/\partial y^* > 0 \mathrm{or} C_y < 0 \rangle$). We obtain the state named #*P* for the one linked to a positive value of the $\partial C_p/\partial y^*$ and the other named #*N* associated with the negative one. The conditional averaged velocity and the $\partial C_p/\partial y^*$ or C_y are shown in Fig. 4(b). The typical time-history of both $\partial C_p/\partial y^*$ and C_y, filtered using a zero-phase low pass filter, show a similar behavior with nearly synchronized time events occurrences. It demonstrates that flow bistability induces side-force variations due to the pressure center switching from left to right (or right to left) side of the body.

C. Wake-flow-topology–induced bistability

The first aims of this section is to determine the present critical threshold leading to the bistable state for our configuration. Moreover, considering the parametric study of Cadot *et al.* [17], for a given w/h ratio, both the Reynolds number and the ground clearance affect the onset of the bistability. The bifurcation diagrams against the ground clearance obtained by these authors with different Reynolds numbers show that the bifurcation threshold varies from $g_c/w = 0.11$ at $\mathrm{Re}_{h_c} = 1.78 \times 10^4$ to $g_c/w = 0.075$ at $\mathrm{Re}_{h_c} = 1.6 \times 10^5$. Then the critical ground clearance slowly decreases as $\mathrm{Re}_{h_c}^{-1/6}$ with the critical Reynolds number. Consequently, for the present study, five PIV flow cases (Fig. 3) are considered (reported in Table III) and are focused on the critical threshold of our configuration with central support. These cases are chosen to analyze both Reynolds and ground-clearance effects on the wake-flow dynamics with and without wake bistability. Figure 5 shows the five considered cases with the streamlines and the separatrix line. The critical case connected with the onset of the bistability has been identified for $\mathrm{Re}_h = 2.86 \times 10^5$ and corresponds to a critical ground clearance of $g_c/w = 0.1$. As previously pointed out by Grandemange *et al.* [3], the influence of the ground proximity is very important since it drives the under-body flow and the interactions with the wake. The main goal of this paper is to deeply investigate these interactions with regards to the under-body flow rate condition depending on the Reynolds number and the ground clearance. The normalized under-body velocity profiles are plotted in Fig. 5 for the different studied cases to compute the under-body mean flow velocity, U_s^* and the corresponding under-body flow rates, $q_s^* = g^* U_s^*$ reported in Table III. As previously discussed, due to the central support used to mount the Ahmed body, the comparison with other studies that uses different mounting support is not easy. This can be seen in Fig. 5 where the maximum velocity is only $0.7U_\infty$, while in Cadot *et al.* [17], the maximum velocity saturates to $1.1U_\infty$. It indicates that the wake of the central support reduces considerably the flow at the bottom edge of the base. Thus it is not possible to have a direct comparison with some of the other studies reported in Table I. Nevertheless, the present investigation is still adapted to investigate the wake around the present defined clearance threshold. As shown in Fig. 5, for very small g/w, up to 0.1, the viscous effect dominates and decreases the under-body flow rate. The under-body flow exists but is not sufficiently strong in comparison with the external flow to be able to generate high momentum that prevents the boundary layer separation on the

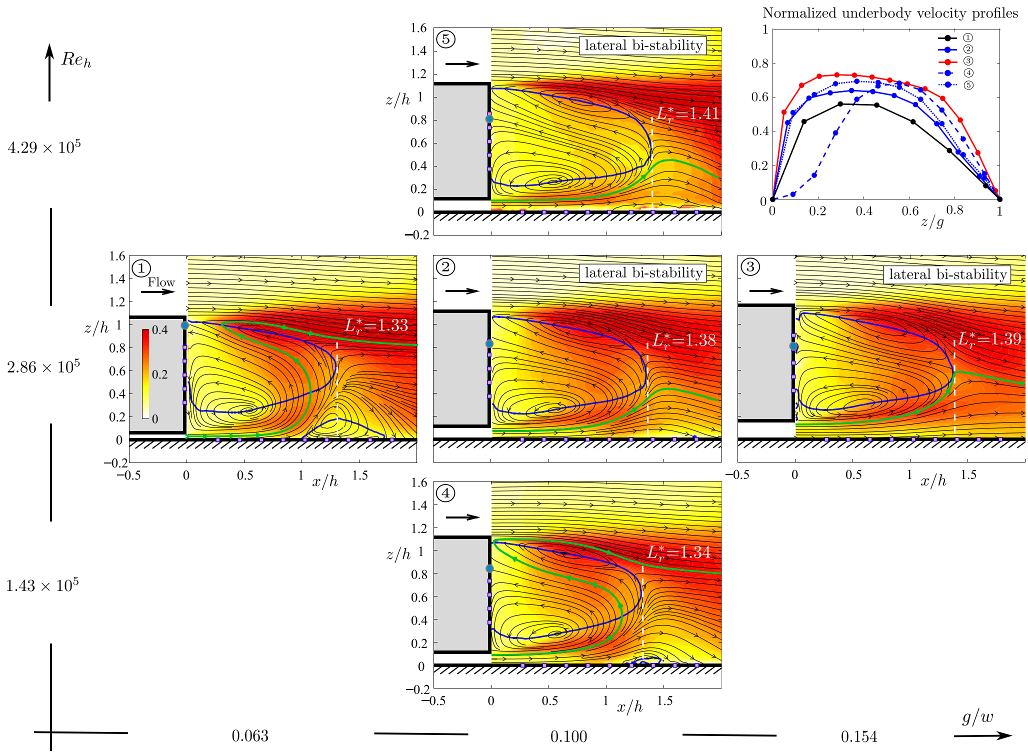

FIG. 5. Root-mean-square velocity magnitude fields normalized by the free-stream velocity with time-average streamlines from PIV measurements for different Reynolds numbers and ground-clearance ratios. The blue line denotes the mean separatrix lines. Cyan circle symbol denotes the zero vertical velocity location (taken at $x/h = 0.02$). The selected streamline, depicted in green, highlights the typical underflow behavior for each case. The right top figure gives the normalized under-body velocity profiles (extracted from PIV measurements) used to compute the normalized mean under-body flow velocity, U_s^*, reported in Table III.

ground. This separation can be shown in Fig. 5 for $g/w = 0.063$ and occurs for $1 < x/h < 1.8$. In this case, the under-body flow strongly interacts with the reversed wake bubble and changes the connected flow topology. In particular, the size of the back flow structure close to the ground is larger than the upper one, mainly due to the weak influence of the under-body flow in comparison to the external upper flow. At this point, no wake symmetry breaking phenomena is observed. For $g/w > 0.1$, the under-body flow rate is sufficiently high to suppress the ground separation and the under-body flow rate has approximately the same order of magnitude than the upper one (see Fig. 5 for $g/w = 0.154$). In this case, a bistability behavior is observed and is connected with the slight upper flow interactions with the reversed bubble. The phenomenon increases the wake sensibility to external flow perturbations. For a same g/w, an increase of the Reynolds number can also lead to similar conclusion. The evolution of the flow topology can be easily observed in Fig. 5 against the Reynolds numbers and can be correlated with the repartition and the magnitude of the RMS velocity. The zero vertical velocity locations (cyan circle symbol) in the middle plane taken at $x/h = 0.02$ are also reported in Fig. 5. The under-body flow interactions with the base of the body can be underlined and identified by this mean as discussed later. The decreasing of the zero vertical velocity location induces an extension of the wake that can be quantified by an increase of the reattachment length, L_r. So, the larger the Reynolds number is, the larger the base suction is and it related to a drastic change of the flow topology around the onset of the instability. When the instability is fully developed (i.e., with an under-body flow of about $0.7U_\infty$ along the ground-clearance gap), the larger the Reynolds number is, the smaller the base suction (or the drag) is, as reported by Barros *et al.* [24]. Moreover, the top and bottom mean vortex cores positions associated with the local minimum of the static pressure (see Fig. 2), are also a function of the g/w and Re_h parameters and have a significant effect on the drag. As discussed previously the minimum of the global drag is associated with the critical case reported in Fig. 2 [i.e., for $\mathrm{Re}_h = 2.86 \times 10^5$ at $g_c/w = 0.1$ or for $q_{sc}^* \approx 0.066$ (see Fig. 5)]. Consequently, the onset of the bistability phenomenon is linked to the under-body flow interaction with the reversed wake bubble as highlighted by the selected green streamline shown in Fig. 5. Indeed, when strong interactions are observed, an unimodal PDF distribution of the lateral pressure gradient is also observed and in the case of a bimodal distribution, only a weak interaction between the under-body flow and the wake can be observed. This low level of interaction leads to a higher sensitivity of the wake flow to external perturbations than in the case of a strong interaction where the under-body flow maintains, through this interaction, the lateral wake-flow stability. As a conclusion of this preliminary part of the study, it is important to notice that our experimental setup allows demonstrating the effect of the topology changes due to the onset of the bistability and that the central model support has a significant influence on the critical bistability onset threshold and the associated drag reduction. The following parts of the study focus on this point and provide, for a chosen Reynolds number of $\mathrm{Re}_h = 2.86 \times 10^5$, more details about the global wake interactions as a function of the ground clearance.

IV. WAKE-FLOW INTERACTIONS

The drag reduction mechanism connected with the wake-flow structure transition is investigated in this section. A detailed description of the formation and subsequent evolution of the shear-layer vortex structures linked to wake shear-layers interactions with the under-body and the incoming side flows are also given. In the following, since the Re_h is set to 2.86×10^5, only the ground-clearance parameter will be used to modulate the wake-flow behavior. The corresponding under-flow rates are reported in Table III.

A. Top shear-layer and under-body flow coupling

First, we analyze the instantaneous velocity fields in the middle plane **x-z** for the three studied g/w ratios to highlight the flow interactions depending on the under-body flow conditions. A proper orthogonal decomposition (POD) filtering (see Appendix for details) retaining 300 first modes is applied to suppress the residual noise and the very small vortices related to turbulence. Normalized instantaneous velocity field magnitudes are shown in Fig. 6. Three flow cases (or classes) can be defined as previously proposed by Castelain *et al.* [30] for simplified truck model depending on the under-body flow. The following three cases of interaction must be considered for the present Ahmed body configuration;

(1) Case (**I**), the under-body flow rate is very low ($q_s^* < 0.066$). In this case, a stationary vortex structure (denotes by S_{VC} in Fig. 6) is located at the bottom of the wake. The weakness of the under-body flow rate induces a deflection due to lateral incoming flows. This flow conditions are connected with a strong incoming flow from the bottom inside the wake as shown in Fig. 6 for $g/w = 0.063$. We can observe from the instantaneous velocity fields that the upward flow can interact with the top shear-layer either directly to the shear-layer generating large structures (**Ia**) or at the beginning of the shear-layer amplifying the Kelvin-Helmholtz oscillation and the associated shear-layer shedding (**Ib**). The dynamical behavior is connected with a one side shear-layer shedding. In this case no lateral bistability is observed and the mean pressure coefficient at the back of the body is maximum close to the top edge. The corresponding $C_{p_{\mathrm{rms}}}$ distribution is homogeneous and does not show specific fluctuating activity.

(2) Case (**II**), the under-body flow rate is slightly higher that in the case (**I**) typically for $q_s* \approx 0.066$. This flow configuration induces a movement of the bottom vortex core (denoted by M_{VC} in Fig. 6) in the flow direction and reduces the lateral incoming flow as observed in the case (**I**)

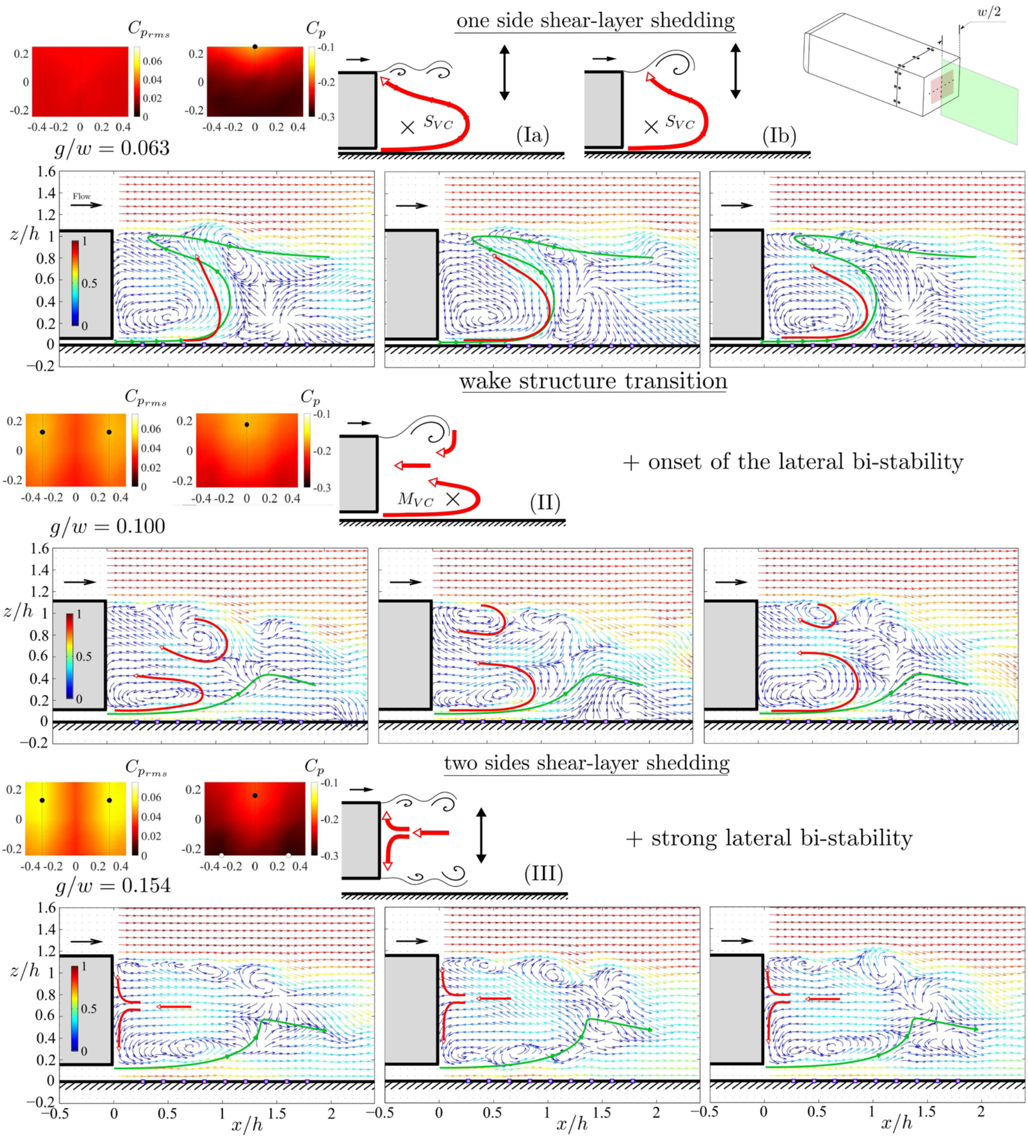

FIG. 6. Sample of normalized instantaneous velocity magnitude frames in the middle plane *x*-*z* showing evolution of flow structures. A POD filtering (retaining 300 first modes) is applied. To have an idea of the mean underflow stream behavior, the mean selected streamline, depicted in green in Fig. 5 is also reported in the present figures. S_{VC} and M_{VC} indicate the stationary and moving vortex core positions.

allowing the onset of lateral bistability as pointed out by the two peaks of the $C_{p_{\mathrm{rms}}}$ distribution in Fig. 6 for $g/w = 0.1$. A back flow behavior decreasing the C_p minimum location ($z = 0.19h$) is also observed. We can notice that, in this configuration, the value of the mean pressure coefficient is globally higher than in the case (**I**). This flow configuration can be considered as a wake-flow structure transition between the case (**I**) and the case (**III**) described hereafter.

(3) A high under-body flow rate ($q_s^* > 0.066$) related to the case (**III**) is shown in Fig. 6 for $g/w = 0.154$. In this case the weak wake/underflow interactions lead to a more classical symmetric behavior of the bottom/top shear-layers. Two sides shear-layers shedding phenomena are observed

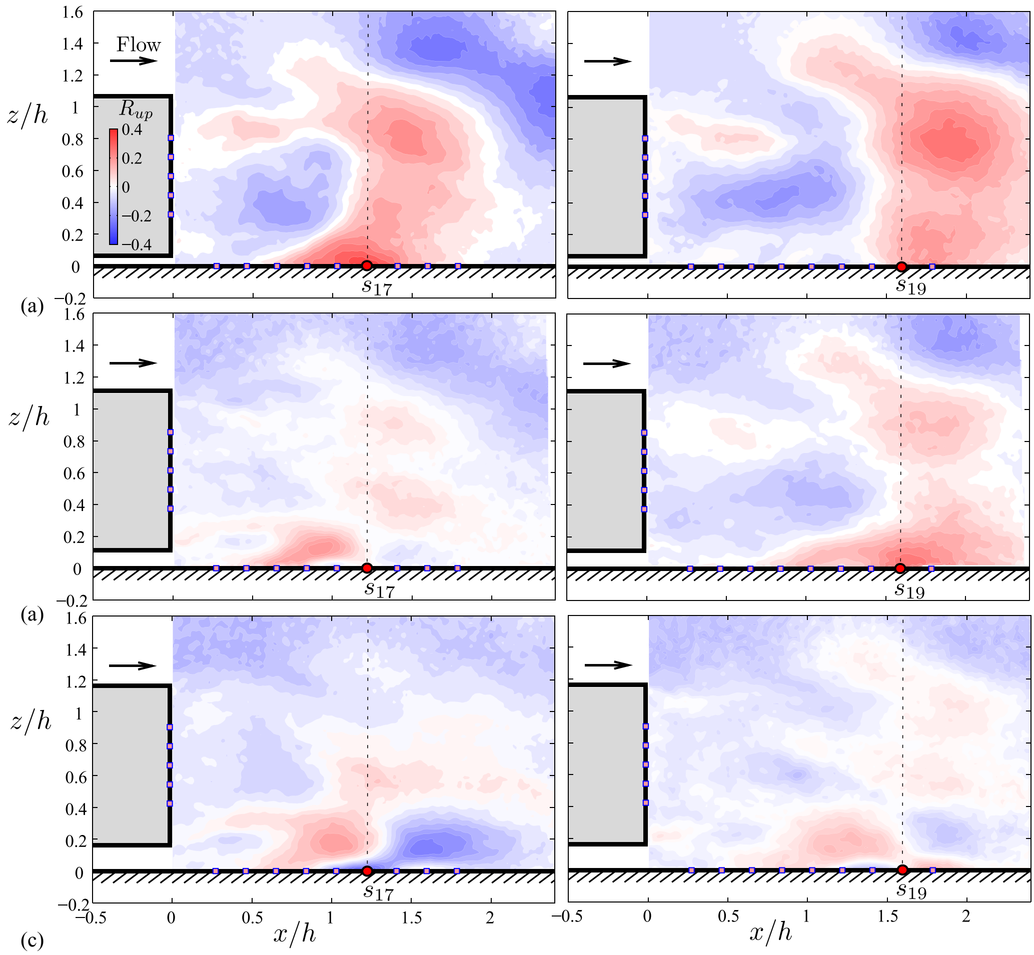

FIG. 7. Spatiotemporal pressure/velocity correlations fields, R_{up}, computed between PIV velocity fields and the wall pressure sensors s_{17} and s_{19} in the vertical middle plane for (a) $g/w = 0.063$, (b) $g/w = 0.100$, and (c) $g/w = 0.154$ at $\text{Re}_h = 2.86 \times 10^5$.

and lateral incoming flow due to bistability phenomenon in the plane **x-y** highlights a back flow behavior decreasing the C_p minimum location ($z = 0.17h$). Strong $C_{p_{\text{rms}}}$ peaks describing a high fluctuating bistable process are also observed in this configuration.

The present wake-flow interactions have a significant impact on the oscillation global mode (black arrows in Fig. 6). Furthermore, spatiotemporal pressure/velocity correlations defined as $R_{\text{up}} = \frac{<u(t)p(t)>}{u_{\text{rms}}p_{\text{rms}}}$, are computed between the concomitant PIV frames and unsteady pressure measurements to investigate the global antisymmetric periodic wake modes of Ahmed body occurring in the **x-z** plane. Figure 7 shows the spatiotemporal pressure/velocity correlations fields, R_{up} with the PIV measurements and the pressure probe s_{17} (respectively, s_{19}) for the three g/w cases. Results for the two pressure locations demonstrate that for the lowest g/w ratio [see Fig. 7(a)], a strong correlation exists between the flow close and far from the wall, and suggests a large scale global one side shear-layer shedding behavior described previously. This behavior is still present for the middle g/w ratio [see Fig. 7(b)], but with lower correlation levels and totally disappears for the higher g/w ratio [see Fig. 7(c)], suggesting a two side classical shedding mechanism. R_{up} and R_{vp} profiles are also plotted in Fig. 8 following the dash-dot line plot in the correlation map of the Fig. 7. Results

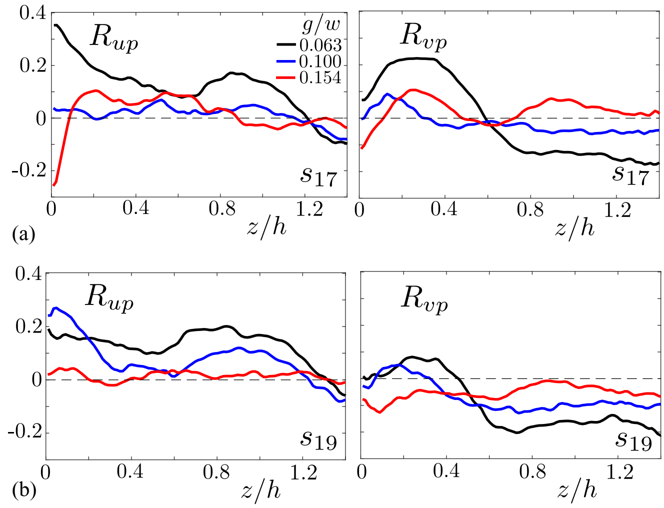

FIG. 8. Profiles of R_{up} and R_{vp} following the dash-dot line plot in Fig. 7 for the three present g/w cases and for the two sensors (a) s_{17} and (b) s_{19}.

confirm this behavior by the presence of correlation peaks and underline the asymmetric characters of the periodic wake modes in the **x-z** plane for the higher g/w ratio where the R_{uv} correlation sign changes depending on whether we are near or far from the wall (black curves R_{vp} profiles in Fig. 8).

B. Lateral shear-layers interactions

To have more information about the transversal wake dynamic in the case of WSB, normalized velocity amplitude fields showing evolution of flow structures corresponding to the #*N* mode are presented in Fig. 9 for $g/w = 0.154$. The same low order filtering used previously is also employed on the instantaneous transverse PIV fields. The vortex core structure of interest is marked with an **A** or **B** for three selected consecutive time instants named t_1 to t_6 corresponding to the #*N* mode. The results clearly show a quite static behavior of the structure **B** and a shear-layer vortex shedding on the opposite side (**A** structures). More generally, a very similar wake organization can be observed for the #*P* mode as shown in Fig. 9 where two vortical structures located close to the shear-layer. To clarify this phenomena, for each state (#*P* and #*N*), the location of the vortical cores is determined by applying the Γ_1 criterion proposed by Graftieaux *et al.* [31] and only the strong events are retained for the comparison. The results for both cases (#*P* and #*N*) with the associated time-averaged streamlines are reported in Fig. 10 and demonstrate the preferential shear-layer shedding phenomenon previously described. A scheme of the lateral dynamic behavior is also shown in Fig. 9 and highlight the one side shear-layer amplification principle linked to the incoming flow from the other side.

To further elucidate the link between the un-stable pressure characteristics at low-frequency and the associated shedding phenomena, the spatiotemporal pressure/velocity correlations are computed. These correlations are obtained using simultaneous unsteady pressure and PIV data (or hot-wire measurements) in the wake. Space-time correlations are computed to quantify the main flow structure footprints and confirm the main flow mechanism playing a key role on the bistability process. First of all, the correlations between the vertical middle PIV plane and the pressure probe, s_{13} are plotted on the two top Figs. 11(a) and 11(b). The interaction mechanism between the underflow and the wake is here clearly indicated by the high degree of correlation in the case $g/w = 0.063$ compared to the low correlation observed for $g/w = 0.154$. In the same way, the bottom Figs. 11(a) and 11(b) depict the correlation in the transverse middle PIV plane and the

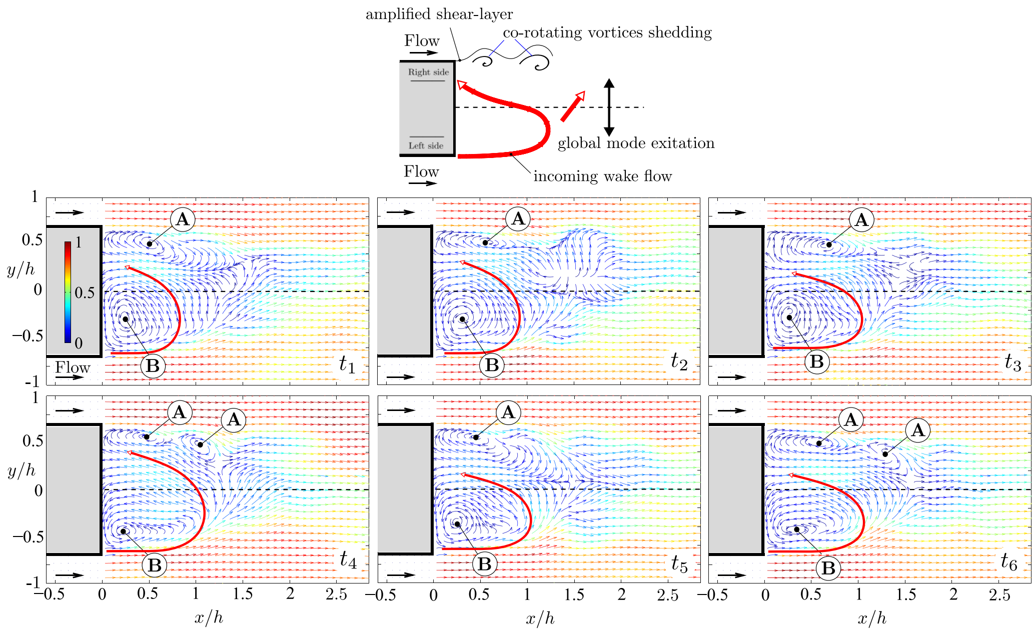

FIG. 9. Sample of normalized instantaneous velocity magnitude frames in the middle plane x-y showing evolution of co-rotating shear-layer vortices corresponding to the #*N* state. The time between successive frames is, $t = 14h/U_\infty$. A POD filtering (retaining 300 first modes) is applied.

sensor s_6. In the unstable case ($g/w = 0.154$), the high degree of correlation highlights the WSB modes with a phase opposition between the two side of the body. Comparatively, for the stable case ($g/w = 0.063$) only low correlation level can be observed. The correlation area underlines a bidimensional reorganization of the wake occurring for $g/w \approx 0.1$ with relatively slight transversal effect highlighted by the spanwise correlation observed. This flow topology reorganization can be compared to those observed by Bailey *et al.* [32] for a square cylinder in cross-flow with wall interactions. This phenomenon, due to the wall interactions, explains how the external flow impacts the wake topology dominant structures and can break the existing top/bottom equilibrium in the wake. Considering now only the bistable case to better understand the nature of the motions connected with short-time wake dynamics, the coherence between pressure signals recorded at the rear back of the body and the hot-wire unsteady velocity measurements in the wake of the model are

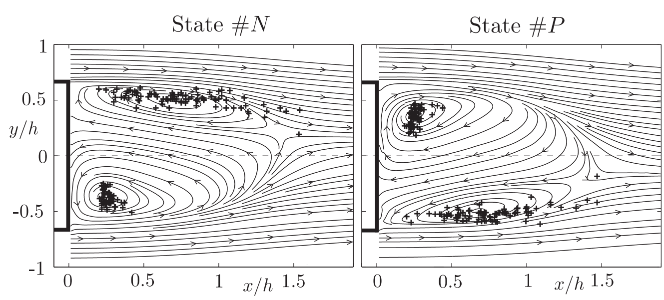

FIG. 10. Vortex center locations for the states #*N* and #*P* using the Γ_1 criterion proposed by Graftieaux *et al.* [31]. The conditional time-average streamlines are also reported for clarifying the mean structures background for each state.

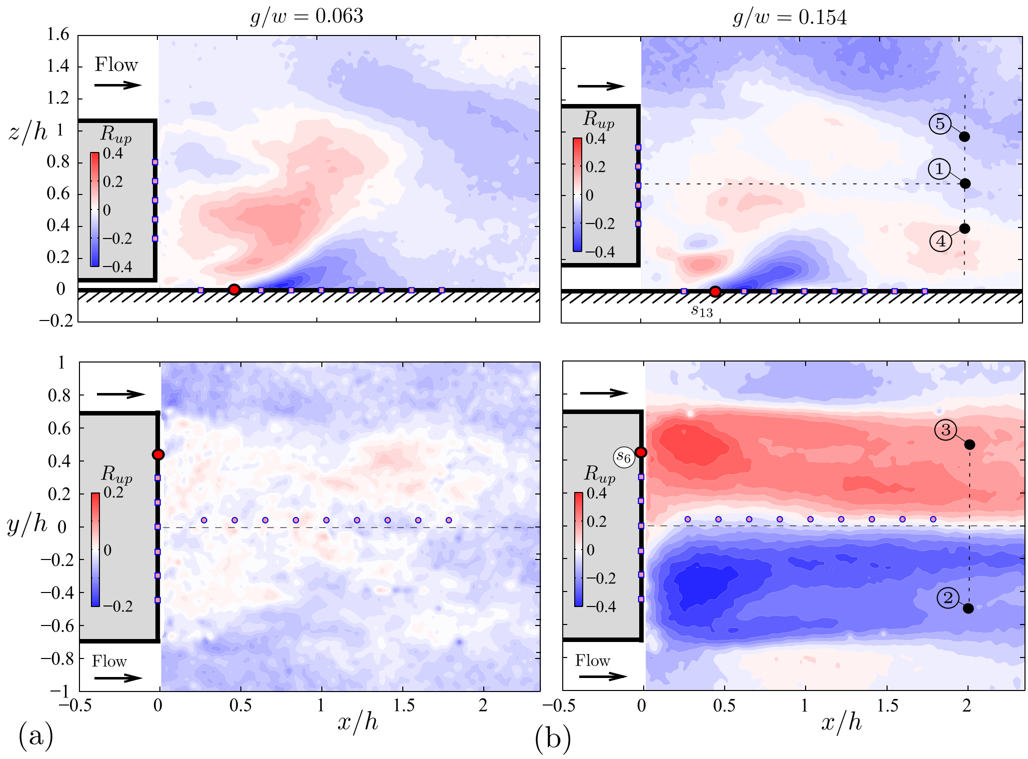

FIG. 11. Spatiotemporal pressure/velocity correlations, R_{up}, computed between the PIV velocity fields (a) in the vertical middle plane and the pressure sensor, s_{13}, (b) in the transverse middle plane and the pressure sensor, s_6, respectively, for $g/w = 0.063$ and 0.154 at $\mathrm{Re}_h = 2.86 \times 10^5$.

considered, following the approach used by Duell and George [33] and more recently by Pavia *et al.* [34] and Volpe *et al.* [19]. The magnitude of the coherence between two synchronized velocities and pressure signals is calculated according to the equation, $C_{\mathrm{up}}(f) = \frac{|P_{\mathrm{up}}(f)|^2}{P_{\mathrm{uu}}(f)P_{\mathrm{pp}}(f)}$, where $P_{\mathrm{up}}(f)$ is the cross-spectrum, $P_{\mathrm{uu}}(f)$ and $P_{\mathrm{pp}}(f)$ are the auto-spectra of the velocity and the pressure signal, respectively. Local coherence can also give some interesting information about the shedding process and the convective motions for the bistable case. Indeed, we can observe a good level of correlation between the pressure sensor, s_6 and the velocity sensor 3 located at the right side of the body with a clear peak at $\mathrm{St}_h = 0.13$ [see Fig. 12(a)]. This high energetic peak confirms the lateral antisymmetric periodic global mode. Another peak around $\mathrm{St}_h \approx 0.5$ is also observed and can be associated with the shear-layer lateral shedding.

Toward the wall of the model, the correlation between the pressure sensor located at the floor close to the rear surface of the body and the velocity sensor 4 in the bottom wake shows another strong peak at $\mathrm{St}_h = 0.18$. This last peak, only visible at the top or at the bottom of the model, can clearly be connected with the vertical shedding motion as previously suggested. The pressure cross-correlation between the pressure sensors s_{12}/s_{13} and also between s_{13}/s_{14} plotted in Fig. 12(b) exhibits a strong correlation peak at a quite constant time delay $\tau^*_{\mathrm{peak}} \approx 0.35$, underlining the convective motion of the flow structures coming from the underbody as discussed earlier. The spatiotemporal pressure/velocity correlation between the pressure sensors s_{13} and the velocity probe located at the bottom side of the wake is showed in Fig. 12(c). The shape of the correlation is typical of a quasi-periodical phenomena with an approximate period, $T^* = 5.5$ corresponding to the shedding frequency previously obtained. When left-to-right opposite probing

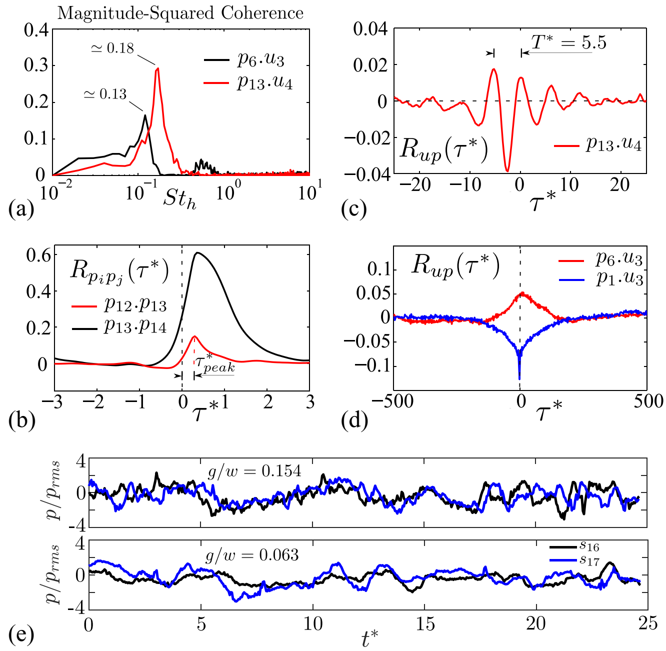

FIG. 12. For the case, $g/w = 0.154$, (a) magnitude-square coherence between the pressure sensors, (b) pressure cross-correlation, (c, d) spatiotemporal pressure/velocity correlations, (e) normalized wall pressure time-histories.

locations are considered [see Fig. 12(d)], it is found that the pressure-velocity fluctuations show a strong correlation with a phase opposition. This is another confirmation of the left-to-right bistable behavior of the wake. All these measurements allow us to propose a schematic representation of the wake-flow dynamics associated with stable and unstable lateral flow configuration. In addition, the time histories of the pressure probes s_{16} and s_{17} located close to the separated area at the floor are plotted for $g/w = 0.063$ and 0.0154 in Fig. 12(e). Some back-flow events can be clearly observed for the $g/w = 0.063$ ratio where the local time delay between the two signal can be either positive or negative. For the case $g/w = 0.0154$, the delay between the two signals is all the time positive as shown in Fig. 12(e). Results confirm the unsteady separation process induced by the lateral incoming flow occurring for the lowest g/w ratio.

V. GLOBAL DISCUSSION ABOUT THE OSCILLATING MODES

As ground clearance affects wake-flow dynamics, it also impacts global modes. To quantify the main global antisymmetric periodic modes, a spectral analysis is performed using a hot-wire probe located at $2h$ from the rear surface of the body (according to the recommendation given by Grandemange *et al.* [13]). Some of the most interesting spectra from the hot-wire measurements (probes 2 and 5) are presented in Fig. 13. The colored lines represent the autopower velocity spectra for $g/w = 0.154$ and 0.063 and for the three Reynolds numbers studied. Energetic peaks can be easily identified from autopower velocity spectra and are reported in Table IV for all the measurement locations (probes 1 to 5). These frequencies correspond to vortex shedding timescales related to top/bottom and lateral shear-layer interaction, and are typically observed in the literature for bluff body wakes in the case of WSB [19,27,29]. The values reported in the literature correspond to a top/bottom antisymmetric global mode with a characteristic length scale of $\mathrm{St}_h \simeq 0.174$–$0.19$ and to the similar lateral phenomenon with a characteristic length scale of

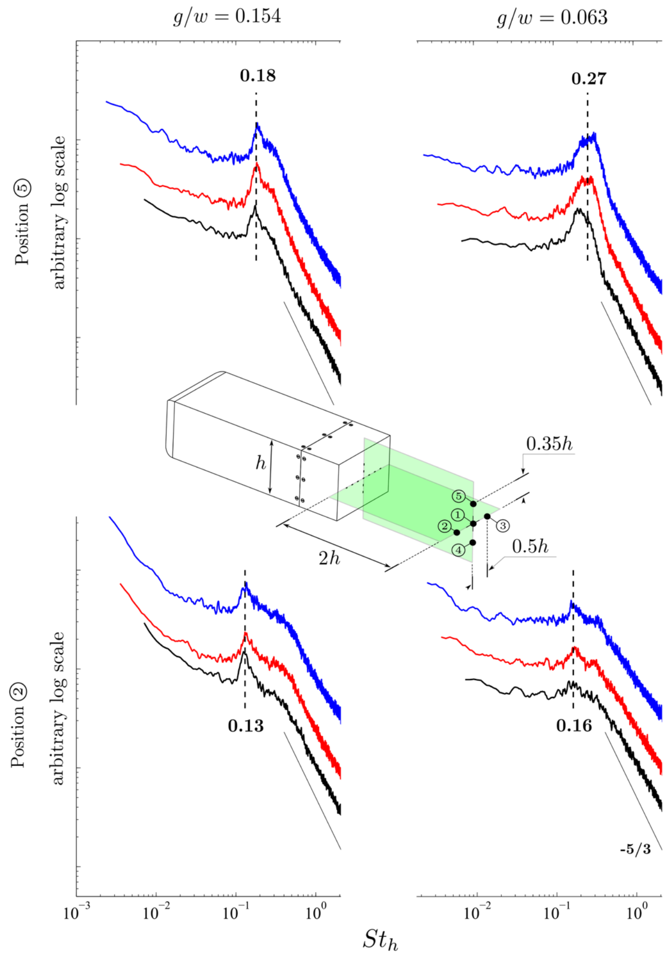

FIG. 13. Autopower velocity spectra in the wake at the position 2 and 5 for $g/w = 0.063$ and 0.154 at $\mathrm{Re}_h = 1.43 \times 10^5$ (black curve), $\mathrm{Re}_h = 2.86 \times 10^5$ (red curve), and $\mathrm{Re}_h = 4.29 \times 10^5$ (blue curve), obtained using hot-wire probe.

$\mathrm{St}_h \simeq 0.127$–$0.13$ ([19,29]). In the present case, we have observed similar frequency peaks values (0.18 and 0.13) systematically for the wall-normal and lateral positions as reported in Table IV. Similar observations can be done using autopower pressure gradient spectra (as shown previously in Fig. 4). For the lateral case, these values can be re-normalized considering the width of the model w, and values close to 0.18–0.2 can be obtained and can be clearly connected with the lateral

TABLE IV. Oscillating global modes frequencies

Hw probe position	$g/w = 0.154$	$g/w = 0.063$
1	0.18	—
2	0.13	0.16
3	0.13	0.16
4	0.18	—
5	0.18	0.27

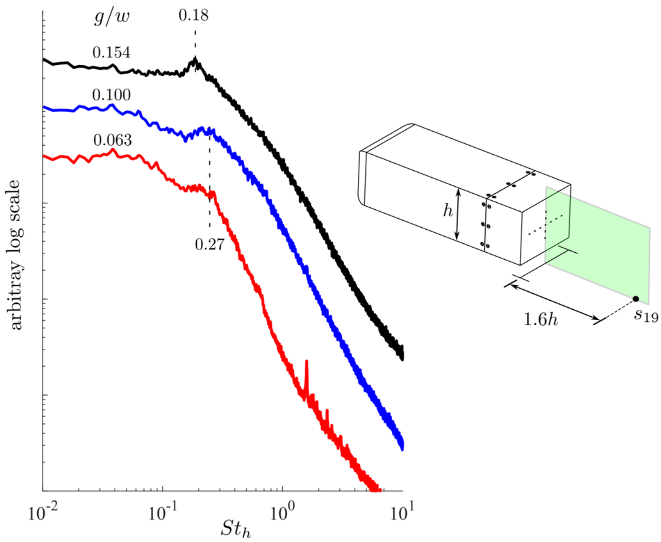

FIG. 14. Autopower wall pressure spectra at $\mathrm{Re}_h = 2.86 \times 10^5$ for the three g/w investigate.

antisymmetric periodic mode. For a lower aspect ratio, Barros *et al.* [27] found also values close to 0.2 confirming the unsteady phenomena. For $g/w = 0.063$ associated with a stable flow topology, different frequency peaks can be observed as shown in Fig. 13. The first observation concerns the significant increase of the frequency peaks value captured on both wake sides connected with a similar lateral mechanism as for the WSB case. This increase can be linked to a reorganization of the wake flow inducing a domination of the downward flow as discussed further. For the hot-wire measurements at the wake center and close to the wall no significant peak is observed contrary to the WSB case. This behavior can be attributed to the weak under-flow rate due to the small ground clearance leading to the boundary layer flow separation on the floor as previously described. The measurements from the upper hot-wire exhibit a strong frequency peak about $\mathrm{St}_h = 0.27$. This high value can be explained by a single shedding phenomena occurring only at the top of the body (as it the case for cylinder in cross flow at the proximity of a wall). Autopower wall pressure spectra at $\mathrm{Re}_h = 2.86 \times 10^5$ for the three studied g/w ratios has also been computed for the probe (s_{19}) located at $1.6h$ from the base of the body and are plotted in Fig. 14. Similar frequency peaks can be observed. The transition from 0.18 to 0.27 can be also shown for the lower g/w to the higher aspect ratio confirming the transition process.

VI. CONCLUDING REMARKS

A combined wall pressure/velocity analysis of the wake of an Ahmed body has been presented in this paper. After a full parametric characterization of the base flow and a discussion of the earlier literature works, a focus is done on two different ground-clearance configurations leading to strong flow topology variations. In particular, the importance of the under-body flow rate (modulated here by variation of the ground clearance) as a key parameter to the onset of the bistability is here highlighted. It can also be noticed that the model support need to be taken into account since it can also strongly affect the under-body flow rate, which in turn impacts the critical bistability onset threshold. The bistability leading to strong interactions between the underflow and the wake shear-layer is at the origin of a substantial drag reduction. The two selecting ground clearances, $g/w = 0.063$ and 0.154 corresponding to a stable and a bistable wake flow were analyzed in detail with a particular interest on the induced unsteady global modes phenomena. In the bistable situation, the present results confirm the previous observations showing the existence of two natural

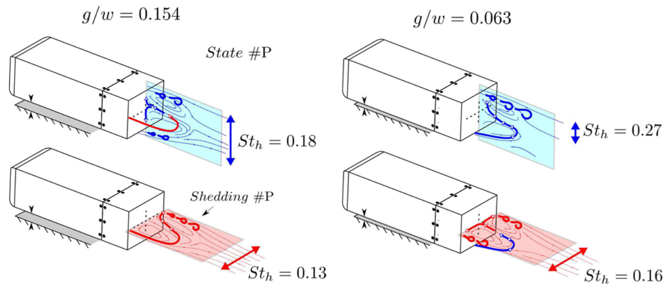

FIG. 15. Schematic representation of the proposed interpretation for the dynamical wake behavior in the case of lateral bistability (herein #*P* mode) and for the stable lateral case ($g/w < 0.100$).

antisymmetric periodic global mode phenomena; the first one associated with the top/bottom wake oscillations and the other related to lateral motions. The main contribution of the present work is to show that the unsteady wake behavior is highly altered by the modulation of the ground clearance. These strong time-space flow topology modifications can be clearly associated with a reorganization of the three-dimensional wake flow due to wall interactions leading to a significant drag reduction previously observed by Bonnavion *et al.* [28]. For information, no low frequency activity at $\mathrm{St}_h \approx 0.07$–$0.08$, which was previously associated by few authors to a “bubble pumping” phenomenon or vortex shedding nonlinear interactions, has been detected for the bistable case. Only a broadband frequency peak has been potentially detected in this frequency range for the lower g/w ratio (see Fig. 14).

All this information enrich the dynamical model of Grandemange *et al.* [13] and allow a more accurate description of the unsteady wake phenomena. The Fig. 15 illustrates the present proposed interpretation for the preferential interaction principle in the case of WSB (mode #*P*) and for the stable case flow configurations, as follows:

(1) For the cases with a ground-clearance ratio (or an under-body flow rate) higher than the critical value (Fig. 15, left), the shear-layer vortex shedding in the transverse plane depends on the flow state, and it occurs only on the opposite side where the smallest recirculation area is formed due to incoming side flow interaction. The corresponding antisymmetric periodic global mode have Strouhal numbers for oscillations of 0.13. In the vertical plane, two side shear-layer vortex shedding occur and the lateral side incoming flow induces a back flow impacting on the base of the body and inducing a significant increasing of the base pressure. The corresponding antisymmetric periodic global mode has Strouhal numbers for oscillations of 0.18 as previously mentioned in the literature.

(2) For the cases with a ground-clearance ratio (or an under-body flow rate) lower than the critical value (Fig. 15, right), the vortex shedding in the vertical middle plane only occurs at the top shear-layer due to strong underflow interaction with the wake. This interaction affects the corresponding antisymmetric periodic global mode and leads to a higher Strouhal number for oscillations of about 0.27 clearly visible only in the top position of the wake. Concerning the transversal flow dynamic, a two side shear-layer shedding occurs and under flows incoming lead to back flow at the base of the body. This phenomenon is similar to that described in the vertical plane for the previous case with a ground-clearance ratio higher than the critical value. The corresponding antisymmetric periodic global mode have Strouhal numbers for oscillations of 0.16.

(3) For the transition case ($g_c/w \approx 0.100$ or $q_s^* \approx 0.066$ for $\mathrm{Re}_h = 2.86 \times 10^5$), the main flow topology feature shows a back flow behavior without too strong bistability negative effect leading to a base pressure increasing in both vertical and transversal plane underlining the global drag reduction observed for this flow configuration.

These preferential interactions mechanisms can be of great interest to better understand the targeting flow topology leading to significant drag reduction to design specific active control strategies.

ACKNOWLEDGMENTS

This work was carried out within the framework of the CNRS Research Federation on Ground Transports and Mobility, in articulation with the ELSAT2020 project supported by the European Community, the French Ministry of Higher Education and Research, the Hauts-de-France Regional Council. The authors gratefully acknowledge the support of these institutions.

APPENDIX: MATHEMATICAL TOOLS

Let us call $u_i(\boldsymbol{x}, t)$ the ith component of the fluctuating velocity field $\boldsymbol{u}(\boldsymbol{x}, t)$ at point $\boldsymbol{x}$ of the spatiotemporal domain Ω and $p_j(t)$ the value of the fluctuating pressure probe $p(\boldsymbol{x}_j, t)$ at point $\boldsymbol{x}_j$ of the boundary spatiotemporal domain $\partial\Omega$. n_s is the number of fluctuating pressure probes and n_c is the number of velocity components of $\boldsymbol{u}$. The ensemble-average of a set of m realizations $\boldsymbol{u}(\boldsymbol{x}, t_i)$ is define as

$$\langle \boldsymbol{u}(\boldsymbol{x}, t)\rangle = \frac{1}{m}\sum_{i=1}^{m} \boldsymbol{u}(\boldsymbol{x}, t_i),$$

and we consider the inner product $\{\boldsymbol{u}, \boldsymbol{v}\}$ and the norm $\|\boldsymbol{u}\| = \{\boldsymbol{u}, \boldsymbol{u}\}^{1/2}$ by

$$\{\boldsymbol{u}, \boldsymbol{v}\} = \sum_{i=1}^{n_c} \int_{\Omega} u_i(\boldsymbol{x}) v_i(\boldsymbol{x}) d\boldsymbol{x}, \qquad i = 1, \ldots, n_c.$$

The POD, also known as principal component analysis or Karhunen-Loeve analysis, is a data analysis method that identifies the dominant structures in a dataset [35–37]. The modal approach is used in the present study to analyze the dynamical aspect of the flow fields. POD is a logical way to build basis functions that capture the most energetic features of the flow. The POD modes are obtained by searching the function $\boldsymbol{\Phi}(\boldsymbol{x})$ that has the largest mean square projection of $\boldsymbol{u}(\boldsymbol{x}, t)$. This maximization problem leads to the well known Fredholm integral problem, where the kernel is the two-point correlation tensor $R_{ij}(\boldsymbol{x}, \boldsymbol{x}') = \langle u_i(\boldsymbol{x}, t) u_j(\boldsymbol{x}', t)\rangle$, where angle brackets is the time-average operator. The integral equation has a discrete set of solutions $\boldsymbol{\Phi}^{(n)}(\boldsymbol{x})$ and λ_n where n is the mode order of the orthogonal decomposition. The eigenfunction are orthonormal, e.g., $\{\boldsymbol{\Phi}^{(n)}(\boldsymbol{x}), \boldsymbol{\Phi}^{(p)}(\boldsymbol{x})\} = \delta_{\mathrm{np}}$. Then the fluctuating velocity field can be decomposed as follows:

$$u_i(\boldsymbol{x}, t) = \sum_{n=1}^{n_m} a^{(n)}(t)\Phi_i^{(n)}(\boldsymbol{x}), \qquad i = 1, \ldots, n_c,$$

where n_m is the total mode number. The temporal coefficients $a^{(n)}(t) = \{\boldsymbol{u}(\boldsymbol{x}, t), \boldsymbol{\Phi}^{(n)}(\boldsymbol{x})\}$ are uncorrelated, e.g., $\langle a^{(n)} a^{(p)}\rangle = \lambda_n \delta_{np}$. More details are given about the POD snapshot method used in the present study in Chovet *et al.* [38].

---

[1] O. Cadot, A. Courbois, D. Ricot, T. Ruiz, F. Harambat, V. Herbert, R. Vigneron, and J. Délery, Characterizations of force and pressure fluctuations of real vehicles, Int. J. Eng. Syst. Model. Simul. **8**, 99 (2015).

[2] S. R. Ahmed, G. Ramm, and G. Faitin, Some salient features of the time averaged ground vehicle wake, Report No. SAE-TP-840300 (1984).

[3] M. Grandemange, M. Gohlke, and O. Cadot, Bi-stability in the turbulent wake past parallelepiped bodies with various aspect ratios and wall effects, Phys. Fluids **25**, 095103 (2013).

[4] D. Barros, J. Borée, O. C. A. Spohn, and B.-R. Noack, Forcing symmetry exchanges and flow reversals in turbulent wakes, J. Fluid Mech. Rapids **829**, R1 (2017).

[5] V. Parezanovic and O. Cadot, Experimental sensitivity analysis of the global properties of a 2D turbulent wake, J. Fluid Mech. **693**, 115 (2012).

[6] R. Brackston, J. G. Cruz de la, A. Wynn, G. Rigas, and J. Morrison, Stochastic modeling and feedback control of bistability in a turbulent bluff body wake, J. Fluid Mech. **802**, 726 (2016).

[7] O. Evstafyeva, A. Morgans, and L. Longa, Simulation and feedback control of the Ahmed body flow exhibiting symmetry breaking behavior, J. Fluid Mech. Rapids **817**, 1 (2017).

[8] B. Khalighi, K.-H. Chen, and G. Iaccarino, Unsteady aerodynamic flow investigation around a simplified square-back road vehicle with drag reduction devices, J. Fluids Eng. **134**, 061101 (2012).

[9] B. Herry, L. Keirsbulck, L. Labraga, and J. Paquet, Flow bistability downstream of three-dimensional double backward facing steps at zero-degree sideslip, J. Fluids Eng. **133**, 054501 (2011).

[10] F. Ravelet, L. Marié, A. Chiffaudel, and F. Daviaud, Multistability and Memory Effect in a Highly Turbulent Flow: Experimental Evidence for a Global Bifurcation, Phys. Rev. Lett. **93**, 164501 (2004).

[11] A. Evrard, O. Cadot, V. H. D. Ricot, R. Vigneron, and J. Délery, Fluid force and symmetry breaking modes of a 3D bluff body with a base cavity, J. Fluids Struct. **61**, 99 (2016).

[12] M. Grandemange, O. Cadot, and M. Gohlke, Reflectional symmetry breaking of the separated flow over three-dimensional bluff bodies, Phys. Rev. E **86**, 035302 (2012).

[13] M. Grandemange, M. Gohlke, and O. Cadot, Turbulent wake past a three-dimensional blunt body. Part 1. Global modes and bistability, J. Fluid Mech. **722**, 51 (2013).

[14] M. Grandemange, M. Gohlke, and O. Cadot, Statistical axisymmetry of the turbulent sphere wake, Exp. Fluids **55**, 1838 (2014).

[15] M. Grandemange, M. Gohlke, V. Parezanovic, and O. Cadot, On experimental sensitivity analysis of the turbulent wake from an axisymmetric blunt trailing edge, Phys. Fluids **24**, 035106 (2012).

[16] E. Varon, Y. Eulalie, S. Edwige, P. Gilotte, and J.-L. Aider, Chaotic dynamics of large-scale structures in a turbulent wake, Phys. Rev. Fluids **2**, 034604 (2017).

[17] O. Cadot, A. Evrard, and L. Pastur, Imperfect supercritical bifurcation in a 3D turbulent wake, Phys. Rev. E **91**, 063005 (2015).

[18] J. Charonko and P. Vlachos, Estimation of uncertainty bounds for individual particle image velocimetry measurements from cross-correlation peak ratio, Meas. Sci. Technol. **24**, 065301 (2013).

[19] R. Volpe, P. Devinant, and A. Kourta, Experimental characterization of the unsteady natural wake of the full-scale square-back Ahmed body: Flow bistability and spectral analysis, Exp. Fluids **56**, 99 (2015).

[20] M. Grandemange, Analysis and control of three-dimensional turbulent wakes: From axisymmetric bodies to road vehicles, Ph.D. thesis, École Polytechnique, ENSTA ParisTech, 2013, https://pastel.archives-ouvertes.fr/pastel-00947364/document.

[21] Y. Eulalie, P. Gilotte, I. Mortazavi, and P. Bobillier, Wake analysis and drag reduction for a square-back Ahmed body using LES computations, in *Proceedings of the ASME 4th Joint U.S.-European Fluids Engineering Division Summer Meeting (FEDSM'14), Chicago, IL* (ASME, New York, 2014).

[22] A. Evrard, O. Cadot, C. Sicot, V. Herbert, D. Ricot, and R. Vigneron, Comparative effects of vortex generators on Ahmed's square-back and minivan car models, Proc. Inst. Mech. Eng., Part D **231**, 1287 (2017).

[23] R. Li, Aerodynamic drag reduction of a square-back car model using linear genetic programming and physics-based control, Ph.D. thesis, ISAE-ENSMA Ecole Nationale Supérieure de Mécanique et d'Aérotechique - Poitiers, 2016, https://www.theses.fr/2017ESMA0014.

[24] D. Barros, J. Borée, B.-R. Noack, A. Spohn, and T. Ruiz, Bluff body drag manipulation using pulsed jets and Coanda effect, J. Fluid Mech. **805**, 422 (2016).

[25] J.-M. Lucas, O. Cadot, V. Herbert, S. Parpais, and J. Délery, A numerical investigation of the asymmetric wake mode of a square-back Ahmed body—Effect of a base cavity, J. Fluid Mech. **831**, 675 (2017).

[26] G. Bonnavion and O. Cadot, Unstable wake dynamics of rectangular flat-backed bluff bodies with inclination and ground proximity, J. Fluid Mech. **854**, 196 (2018).

[27] D. Barros, J. Borée, B.-R. Noack, and A. Spohn, Resonances in the forced turbulent wake past a 3D blunt body, Phys. Fluids **28**, 065104 (2016).

[28] G. Bonnavion, O. Cadot, V. Herbert, S. Parpais, R. Vigneron, and J. Delery, Effect of a base cavity on the wake modes of the square-back Ahmed body at various ground clearances and application to drag reduction, in *Proceedings of the 23rd French Mechanical Congress* (Lille, France, 2017).

[29] M. Grandemange, M. Gohlke, and O. Cadot, Turbulent wake past a three-dimensional blunt body. Part 2. Experimental sensitivity analysis, J. Fluid Mech. **752**, 439 (2014).

[30] T. Castelain, M. Michard, M. Szmigiel, D. Chacaton, and D. Juvé, Identification of flow classes in the wake of a simplified truck model depending on the underbody velocity, J. Wind Eng. Ind. Aerod. **175**, 352 (2018).

[31] L. Graftieaux, M. Michard, and N. Grosjean, Combining PIV, POD and vortex identification algorithms for the study of unsteady turbulent swirling flows, Meas. Sci. Technol. **12**, 1422 (2001).

[32] S. Bailey, R. Martinuzzi, and G. Kopp, The effects of wall proximity on vortex shedding from a square cylinder: Three-dimensional effects, Phys. Fluids **14**, 4160 (2002).

[33] E. Duell and A. George, Experimental Study of a Ground Vehicle Body Unsteady Near Wake, Technical report, SAE technical paper (SAE International, 1999).

[34] G. Pavia, M. Passmore, and C. Sardu, Evolution of the bistable wake of a square-back automotive shape, Exp. Fluids **59**, 20 (2018).

[35] P. Holmes, J. Lumley, G. Berkooz, and C. W. Rowley, *Turbulence, Coherent Structures, Dynamical Systems and Symmetry*, 2nd ed. (Cambridge University Press, UK, 1996).

[36] J. Lumley, The structure of inhomogeneous turbulent flows, in *Atmospheric Turbulence and Radio Wave Propagation*, edited by A. M. Yaglom and V. I. Takarski (Nauka, Moscow, 1967), Vol. 25, pp. 166–178.

[37] L. Sirovich, Turbulence and the dynamics of coherent structures, part I: Coherent structures, Q. Appl. Math. **45**, 561 (1987).

[38] C. Chovet, M. Lippert, L. Keirsbulck, and J.-M. Foucaut, Unsteady behavior of a backward-facing step in forced flow, Flow Turbul. Combust. **102**, 145 (2018).